High-Temperature Materials

SCIEPublish

Article

Fabrication of Gradient Structured $(Ta_{0.2}Nb_{0.2}Ti_{0.2}Zr_{0.2}Hf_{0.2})C$-SiC Composites and Their High-Temperature Ablation Behavior

Xinnuo Wang, Cuiyan Li *, Haibo Ouyang *, Qian Yang and Tianzhan Shen

Key Laboratory for Green Manufacturing & Functional Application of Inorganic Materials, School of Materials Science and Engineering, Shaanxi University of Science and Technology, Xi'an 710021, China; 240211053@sust.edu.cn (X.W.); yq_121297@163.com (Q.Y.); tzshen2243@163.com (T.S.)

* Corresponding author. E-mail: licuiyan@sust.edu.cn (C.L.); ouyanghb@sust.edu.cn (H.O.)

Received: 6 August 2026; Revised: 12 August 2026; Accepted: 14 September 2026; Available online: 20 September 2026

ABSTRACT: Porous high-entropy carbide ceramics (PHECs) exhibit excellent high-temperature stability and are considered promising candidates for thermal-protection applications. However, their interconnected pore structure facilitates oxygen ingress during ablation, resulting in accelerated oxidation and structural degradation. In this work, a gradient SiC-rich dense surface layer was constructed on porous $(Ta_{0.2}Nb_{0.2}Ti_{0.2}Zr_{0.2}Hf_{0.2})C$ ceramics through phenolic-resin infiltration, carbonization, and reactive melt infiltration (RMI) of silicon. The resulting composites exhibited a hierarchical architecture consisting of a dense SiC-rich surface layer and a porous interior. The initial pore structure strongly influenced molten-Si infiltration and reaction behavior, leading to an increase in the thickness of the SiC-rich dense layer from 33.3 to 121.2 μm with increasing porosity. During ablation, oxidation of SiC generated SiO_2, which interacted with refractory transition-metal oxides to form a SiO_2-rich composite oxide layer that effectively suppressed oxygen diffusion and enhanced oxidation resistance. Consequently, the oxide-layer thickness decreased from 121.4 to 35.2 μm, accompanied by a significant reduction in the mass ablation rate. Among all samples, HEC-SiC5 exhibited the best ablation resistance, with a mass ablation rate as low as 0.23 mg/s. This work establishes a direct correlation between substrate pore architecture, molten-Si infiltration behavior, dense-layer evolution, and ablation resistance, providing a practical strategy for the design of lightweight porous HEC-based thermal-protection materials.

Keywords: (TaNbTiZrHf)C; SiC-rich gradient layer; Reactive melt infiltration; Ablation resistance

1. Introduction

Ultra-high temperature ceramics (UHTCs) have emerged as promising materials for critical components of hypersonic vehicles, such as nose tips and leading edges, because of their high melting points, excellent high-temperature stability, and resistance to thermal and oxidative damage [1–4]. Representative UHTCs include carbides, borides, and nitrides, such as ZrC [5], HfC [6], TaC [7], and ZrB_2-

© 2026 The authors. This is an open access article under the Creative Commons Attribution 4.0 International License (https://creativecommons.org/licenses/by/4.0/).

based ceramics [8]. However, conventional monolithic UHTCs generally face a fundamental trade-off between surface protection and weight reduction: densification and the incorporation of protective phases can improve oxidation and ablation resistance, but may simultaneously increase density and thermal conductivity. Therefore, spatially tailoring composition, porosity, and phase distribution has emerged as an effective strategy for integrating surface protection with low-density porous structures [9,10].

High-entropy carbide ceramics (HECs) have attracted considerable attention as a new class of UHTCs because their high configurational entropy, severe lattice distortion, and multicomponent chemical interactions can provide a favorable combination of mechanical and thermochemical properties [11–14]. In particular, transition-metal HECs based on (Hf-Ta-Zr-Nb-Ti)C exhibit high hardness and elastic modulus [15–18], together with excellent oxidation and ablation resistance associated with the development of complex multicomponent oxide scales [19–21]. Ni et al. [22] reported the emergence of a multilayer oxide structure in $(Hf_{0.2}Zr_{0.2}Ta_{0.2}Nb_{0.2}Ti_{0.2})C$ after ablation and revealed cooperative Ti outward diffusion and O inward diffusion during oxidation. Ye et al. [23] demonstrated that this HEC system maintains good high-temperature oxidation resistance in the range of 1073–1473 K owing to the presence of a relatively dense protective oxide layer. Peng et al. [24] further showed that nitrogen substitution in $(Ta_{0.2}Hf_{0.2}Zr_{0.2}Ti_{0.2}Nb_{0.2})C_{0.8}N_{0.2}$ can improve ablation resistance through the creation of a high-strength Hf-Zr-rich framework that impedes oxygen transport.

Despite these advantages, the intrinsic pore structure of PHECs introduces a critical limitation for their application in thermal-protection systems. Open and interconnected pores can provide rapid pathways for oxygen transport into the interior, accelerating matrix oxidation and increasing the risk of structural degradation under severe ablation conditions [25–28]. Surface densification is therefore essential to protecting the porous interior without sacrificing the matrix's low-density porous architecture. SiC is one of the most widely investigated second phases for improving the oxidation and ablation resistance of UHTC-based ceramics because of its high-temperature stability and ability to generate SiO_2 during oxidation [29–32]. Under appropriate oxidation conditions, the SiO_2 generated from SiC can form a viscous protective layer that reduces oxygen transport [33,34]. Williams et al. [35] demonstrated the beneficial role of SiC-derived SiO_2 in improving the oxidation resistance of zirconia-based ceramics. Shen et al. [36] systematically investigated the effect of SiC particle size on the ablation behavior of $(Ta_{0.2}Nb_{0.2}Ti_{0.2}Zr_{0.2}Hf_{0.2})C$-SiC composites and showed that fine SiC particles can promote the development of a continuous oxide layer while increasing thermal conductivity. Wang et al. [37] further reported that incorporation of 10vol% SiC substantially reduced the linear ablation rate of (Hf-Ta-Zr-Nb-Ti)C. These studies clearly establish the effectiveness of SiC as a protective phase in HEC-based composites.

However, most existing HEC-SiC studies have focused on relatively homogeneous SiC-containing composites, in which SiC is distributed throughout the ceramic matrix. Although such a homogeneous architecture can improve oxidation and ablation resistance, it does not fully address the conflicting requirements of a lightweight porous interior and a highly protective surface. Increasing the overall SiC content or densifying the entire matrix inevitably modifies the properties of the whole material, rather than selectively strengthening the region directly exposed to the high-temperature oxidizing environment. A SiC-enriched surface layer combined with a porous interior could, in principle, localize oxidation protection near the exposed surface while maintaining the lightweight porous architecture of the interior. The key scientific challenge, however, is how to controllably construct such a gradient architecture and how the initial pore structure of the PHEC matrix governs Si infiltration, SiC formation, and the resulting protective-layer characteristics [38].

Recent studies on gradient ceramic architectures provide evidence that spatially localized protection can effectively reconcile surface protection with lightweight substrates. Yang et al. [39] demonstrated that constructing a gradient ZrB_2-$MoSi_2$-SiC dense layer within a lightweight porous carbon-fiber composite could effectively suppress oxygen penetration and significantly improve its long-term oxidation and

ablation resistance. Zhao et al. [40] fabricated an Hf-Si-based coating–matrix integrated structure via reactive melt infiltration, in which the matrix densification and phase composition exhibited a gradient along the infiltration direction, thereby improving ablation resistance. These studies demonstrate the potential of gradient architectures for integrating a dense protective region with a lightweight porous substrate. Nevertheless, gradient SiC-enriched structures specifically based on porous high-entropy carbide matrices remain insufficiently investigated.

Based on this, in this paper, the porous $(Ta_{0.2}Nb_{0.2}Ti_{0.2}Zr_{0.2}Hf_{0.2})C$ high-entropy ceramic prepared in the laboratory in the previous stage [41] was used as the matrix. Phenolic resin impregnation was employed to introduce a carbon source into the porous framework, followed by reactive melt infiltration of molten Si to generate SiC *in situ*. By tailoring the porosity of the PHEC matrix, the infiltration behavior of molten Si and the development of the SiC-rich dense layer were systematically investigated. This work establishes a structure-property relationship linking initial pore architecture, Si infiltration, SiC-rich layer growth, oxide-scale evolution, and ablation resistance, providing insight into the design of lightweight porous UHTC systems with enhanced ablation resistance.

2. Materials and Methods

2.1. Materials

In this study, Porous $(Ta_{0.2}Nb_{0.2}Ti_{0.2}Zr_{0.2}Hf_{0.2})C$ high-entropy carbide ceramics (PHECs) with different porosities were fabricated according to our previous work [41]. Briefly, mixed oxide powders were carbothermally reduced and subsequently pressurelessly sintered. The porosity was controlled by adjusting the amount of pore-forming agent added during sample preparation. Five PHEC matrices with porosities of 23.08%, 28.67%, 36.92%, 47.23%, 59.34% were obtained and designated as PHEC-1, PHEC-2, PHEC-3, PHEC-4, and PHEC-5, respectively. The dimensions of the PHEC specimens were Φ30 mm × 10 mm. Phenolic resin (99% purity) was used as the carbon source and thermally decomposed to form carbonized carbon, which served as a reaction component for the subsequent *in situ* generation of SiC during the meltable silicon penetration process. Anhydrous ethanol (with a purity of 99.5%) was used as the solvent to prepare the phenolic resin impregnation solution. Monocrystalline silicon powder (with a purity of 99% and a particle size of approximately 10 μm) was used as the silicon source for the meltable silicon penetration process.

2.2. Preparation of $(Ta_{0.2}Nb_{0.2}Ti_{0.2}Zr_{0.2}Hf_{0.2})C$-SiC Composites

2.2.1. Preparation of $(Ta_{0.2}Nb_{0.2}Ti_{0.2}Zr_{0.2}Hf_{0.2})C$-C composites

Firstly, phenolic resin was dissolved in anhydrous ethanol to prepare a 30% phenolic resin solution. Then, samples with different porosities of PHEC were immersed in the phenolic resin solution and placed in a vacuum pressure impregnation device for cyclic impregnation treatment. After each impregnation, the samples were taken out and dried. The impregnation-drying process was repeated three times to introduce sufficient carbon into the pores. Then, the impregnated samples were placed in an argon atmosphere and subjected to pyrolysis at 1000 °C to convert the phenolic resin into pyrolytic carbon (PyC), thereby obtaining $(Ta_{0.2}Nb_{0.2}Ti_{0.2}Zr_{0.2}Hf_{0.2})C$-C composite materials with a carbon-filled structure.

2.2.2. Preparation of Gradient $(Ta_{0.2}Nb_{0.2}Ti_{0.2}Zr_{0.2}Hf_{0.2})C$-SiC Composites

The $(Ta_{0.2}Nb_{0.2}Ti_{0.2}Zr_{0.2}Hf_{0.2})C$-C composite materials obtained in Section 2.2.1 were placed in a graphite crucible and completely covered with silicon powder with a particle size of 10 μm. Then, in an argon-protected condition, the material was subjected to melt infiltration of silicon at 1450 °C for 1 h. Under high-temperature conditions, the silicon powder melted to form liquid Si, and under the action of

capillary forces, it entered the pores of the HEC-C composite material and reacted *in situ* with the pyrolytic carbon to form SiC. By adjusting the initial porosity of PHEC, the penetration depth of SiC and the thickness of the surface dense layer could be controlled. The resulting samples were labeled as HEC-SiC1, HEC-SiC2, HEC-SiC3, HEC-SiC4, and HEC-SiC5. A schematic illustration of the preparation process is shown in Figure 1.

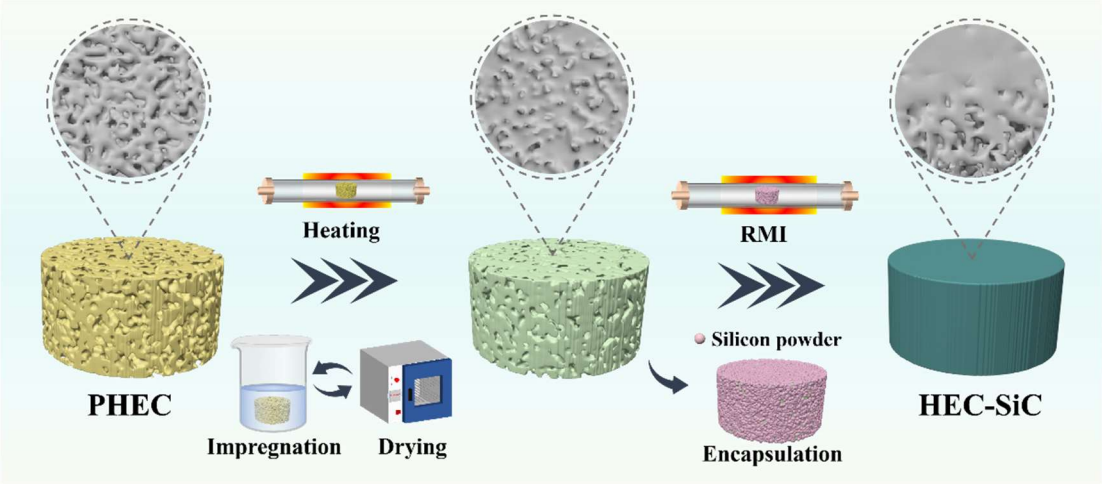


Figure 1. Schematic illustration of the preparation process for the HEC-SiC composites.

2.3. Characterization and Test

The phase composition of the $(Ta_{0.2}Nb_{0.2}Ti_{0.2}Zr_{0.2}Hf_{0.2})C$-SiC composite material and its ablation products was analyzed using an X-ray diffractometer (XRD, D8 ADVANCE-A25, Bruker, Karlsruhe, Germany). A copper target was selected as the target material, with the working scanning range being 20° to 80° and the working scanning rate being 5°/min. The microstructure, pore structure, and SiC distribution of the $(Ta_{0.2}Nb_{0.2}Ti_{0.2}Zr_{0.2}Hf_{0.2})C$-SiC composite material and its ablation products were observed using a scanning electron microscope (SEM, FEIQ45, FEI, Hillsboro, OR, USA), and the element distribution was analyzed in combination with an energy dispersive spectrometer (EDS, EDAX Octane Prime, AMETEK, Mahwah, NJ, USA). Prior to microstructural characterization, all samples were sectioned, ground, and polished to remove any residual surface silicon.

The thicknesses of the SiC-rich dense layer and oxide layer were determined by measuring at least ten randomly selected locations on each sample using ImageJ software. The reported values correspond to the mean thicknesses, and the error bars shown in the column charts represent one standard deviation calculated from the ten measurements.

Ablation tests were carried out using an oxyacetylene flame system at a heat flux of 2.4 MW/m^2. The torch nozzle had an inner diameter of 2 mm and was held at a distance of 10 mm from the sample surface. Cylindrical $(Ta_{0.2}Nb_{0.2}Ti_{0.2}Zr_{0.2}Hf_{0.2})C$-SiC composite specimens (30 mm in diameter, 10 mm in thickness) were exposed to the flame for 120 s. During testing, oxygen and acetylene flow rates were fixed at 0.244 L/s and 0.167 L/s, with pressures of 0.4 MPa and 0.095 MPa, respectively. After ablation, the mass and linear ablation rates were calculated using Equations (1) and (2).

$$R_m = \frac{m_0 - m_1}{t} \quad (1)$$

$$R_l = \frac{l_0 - l_1}{t} \quad (2)$$

where m_0 and m_1 are the mass before and after ablation, respectively; l_0 and l_1 are the thickness of the ablation center area before and after ablation, respectively; And t is the ablation time.

The mass and linear ablation rates were evaluated through three independent ablation tests. For each test, parallel specimens were exposed to identical plasma ablation conditions, and the results are expressed as mean ± standard deviation (n = 3).

3. Results and Discussion

Figure 2 shows the XRD spectra of PHEC samples with different porosities after melt infiltration with silicon. The results indicate that for the HEC-SiC1 sample with a lower porosity, its phase composition mainly consists of high-entropy carbides and SiC. This indicates that when melt infiltration with silicon is carried out at 1450 °C, the molten Si penetrates the pores through capillary action and reacts with the pyrolyzed carbon to form SiC. As the porosity of PHEC increases, molten Si can penetrate more deeply into the porous structure, resulting in more extensive reactions with pyrolytic carbon and consequently a gradual increase in the intensity of SiC diffraction peaks. Meanwhile, the intensity of the Si diffraction peak at approximately 28.4° gradually decreases from HEC-SiC1 to HEC-SiC5. This behavior indicates that increasing porosity promotes the transport of molten Si into the interior of the porous matrix, where it is consumed through the *in-situ* generation of SiC. As a result, the amount of residual Si remaining in the surface region is reduced. In addition, molten Si is highly reactive and, in addition to reacting with carbon, will react with the metal elements in the matrix to form a small amount of high-melting-point metal silicides (such as $TaSi_2$). As the porosity further increases, the amount of SiC formed within the porous structure continuously increases, making the SiC diffraction peaks progressively more dominant. Consequently, the diffraction signals of the high-entropy carbide phase and metal silicides become relatively weaker in the HEC-SiC5 sample. The $HfSiO_4$ diffraction peak in the spectrum can be attributed to trace oxygen impurities present in commercial silicon powder. Under the influence of a lower binding energy, the Hf atoms are most likely to combine with oxygen atoms under the action of high temperature to form HfO_2, and then react with Si to form a small amount of $HfSiO_4$.

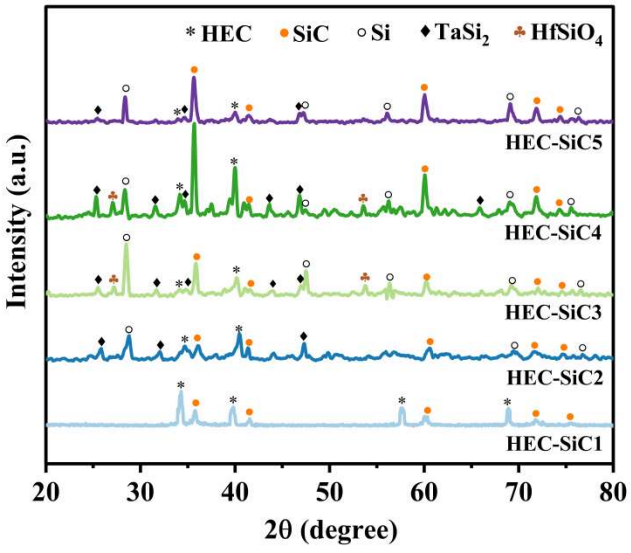


Figure 2. XRD patterns of HEC-SiC1–HEC-SiC5 composites prepared with different initial porosities.

Figure 3 presents the cross-sectional microstructures of the HEC-SiC1–HEC-SiC5 samples obtained by reactive melt infiltration of Si into PHEC matrices with different porosities. The pore morphology of the original PHEC matrices before Si infiltration has been reported in our previous work [35]. All infiltrated samples exhibit a distinct gradient architecture characterized by dense outer regions and a porous interior. During reactive melt infiltration, the specimens were completely embedded in Si powder, allowing molten Si to infiltrate from all exposed surfaces under the combined effects of capillary force and infiltration

pressure at elevated temperatures. Subsequently, the infiltrated Si reacted with the residual pyrolytic carbon within the pores, yielding *in-situ* SiC. Owing to the sufficient supply of molten Si near the surface, SiC nucleated and grew preferentially in these regions, gradually forming SiC-rich densified reaction zones.

With increasing porosity of the PHEC matrix, the interconnected pore network provided more efficient transport pathways for molten Si, thus facilitating deeper infiltration and promoting the generation of SiC. Consequently, the infiltration depth of molten Si and the thickness of the SiC-rich densified reaction zones increased progressively as matrix porosity increased. However, because the *in-situ* generated SiC possesses a high melting point (~2700 °C) and limited atomic diffusivity, the newly formed SiC gradually covered and narrowed the pore channels during infiltration at 1450 °C. This reduced the effective transport flux of molten Si and kinetically hindered its further migration toward the specimen interior. As a result, an outer-dense and inner-porous gradient structure is established after reactive melt infiltration. The outer dense region consists mainly of an HEC-SiC composite phase formed by the reaction between molten Si and pyrolytic carbon, while the interior remains relatively porous.

As shown in Figure 3f, the average thickness of the SiC-rich dense layer increases progressively from 33.3 ± 1.3 μm for HEC-SiC1 to 121.2 ± 1.9 μm for HEC-SiC5 with increasing PHEC porosity. This trend indicates that tailoring the initial pore structure of the porous high-entropy carbide matrix can significantly influence the infiltration of molten Si, the development of the SiC-rich reaction layer, and its thickness.

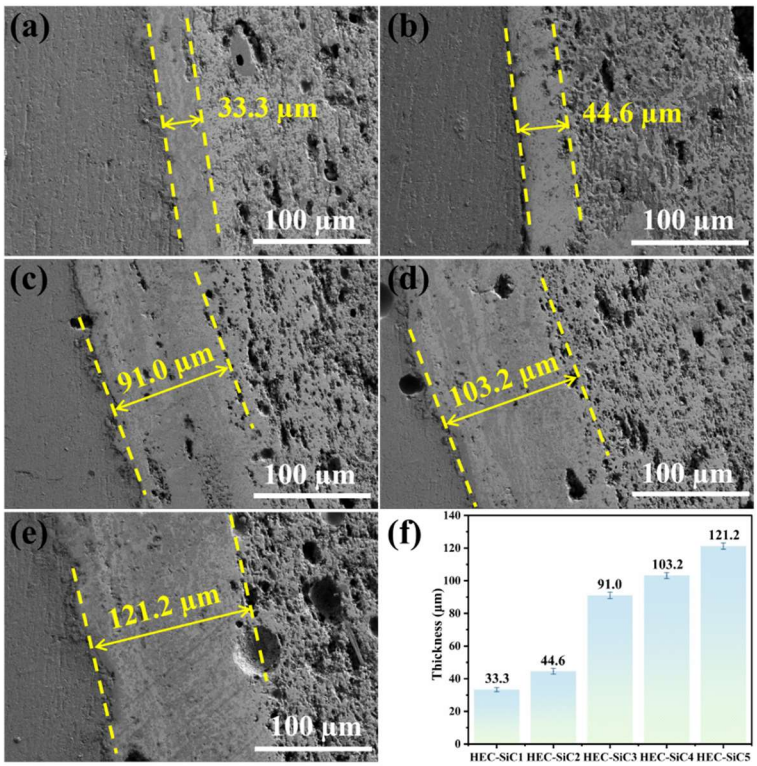


Figure 3. Cross-sectional microstructures of HEC-SiC composites: (**a**–**e**) SEM images of HEC-SiC1–HEC-SiC5 showing the gradient architecture consisting of a SiC-rich dense surface layer and a porous interior; (**f**) Average thickness of the SiC-rich dense layer measured from multiple locations.

In order to further understand the component distribution and microstructure of the samples after melting and silicon infiltration, the cross-section of the HEC-SiC composite material was analyzed using line energy spectrum and elemental mapping. The results are shown in Figure 4. The distribution of seven elements, namely Si, C, Ta, Nb, Ti, Zr, and Hf, is clearly displayed in the figure. In the outermost layer, Si and C elements are significantly enriched, and there is a small amount of transition metals present, indicating that this layer is mainly composed of SiC and trace metal silicides, jointly forming a dense

surface layer. And from HEC-SiC1 to HEC-SiC5, the thickness of this dense layer gradually increases. In the intermediate transition layer, the content of the Si element significantly decreases, while Ta, Nb, Ti, Zr, and Hf transition metals are relatively enriched relative to C elements, indicating that this area is mainly composed of the HEC matrix and forms a composite structure with the infiltrated SiC. In the innermost region, only a trace amount of Si is detected, indicating that the outer SiC-rich dense layer effectively hinders the inward infiltration of molten Si. As a result, this region retains a composition and microstructure similar to those of the original PHEC substrate, confirming the presence of a distinct gradient structure composed of a SiC-rich dense layer and a porous matrix from the exterior to the interior.

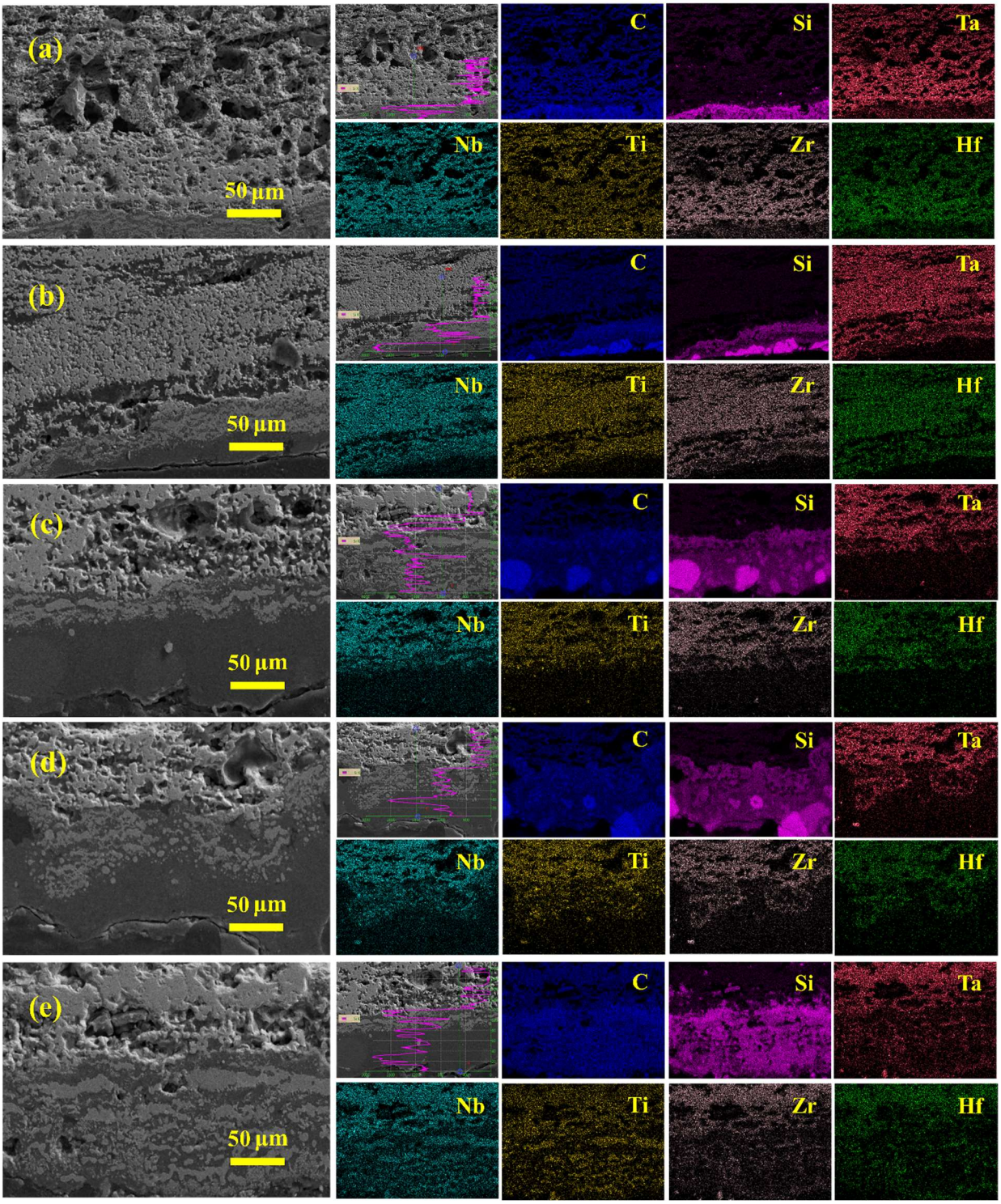


Figure 4. Cross-sectional element distribution diagram of HEC-SiC: (**a**–**e**) correspond to HEC-SiC1–HEC-SiC5, respectively.

Figure 5a is the XRD spectrum of the samples after ablation. The results show that as the thickness of the SiC layer increases, the intensity of the SiO_2 diffraction peak gradually increases, but the overall signal remains weak, indicating that the residual SiO_2 content on the surface after ablation is relatively low. This is mainly due to the influence of the ultra-high flame temperature, where a large amount of SiO_2 evaporates in the form of gas, and only a small amount of SiO_2 can deposit on the surface of the sample. At the same time, obvious composite oxide (Zr, Hf)O_2 diffraction peaks appear in the spectrum, which is due to the reaction of Zr and Hf with oxygen to form ZrO_2 and HfO_2 with lower binding energy, and further solidification under the promotion of high temperature. In addition, under the continuous action of high temperature, the components diffuse with each other and react with oxygen to form high-melting-point complex oxides such as $Nb_2Zr_6O_{17}$, $TaZr_{2.75}O_8$, and a small amount of Ta_2O_5 and (Zr, Hf)TiO_4. These oxides together form a composite oxide layer, which, through the cooperative action of multiple phases, significantly improves the ablation resistance of the material.

The mass ablation rate and linear ablation rate of the HEC-SiC samples exhibit a pronounced decreasing trend from HEC-SiC1 to HEC-SiC5, as shown in Figure 5b. Specifically, the mass ablation rate decreases from 2.39 mg/s to 0.23 mg/s, corresponding to a reduction of approximately 90.4%, while the linear ablation rate decreases from 84.12 μm/s to 10.04 μm/s, representing a reduction of about 88.1%. The consistent variation of these two parameters indicates that the improvement in ablation resistance is reflected in both reduced material loss and suppressed recession of the ceramic surface. This behavior is closely related to the microstructural evolution induced by the different porosities of the PHEC matrices. As discussed previously, increasing the initial porosity promotes the infiltration of molten Si and the subsequent development of a thicker SiC-rich dense layer. The dense layer acts as an effective barrier against the penetration of high-temperature oxidizing species and reduces the direct exposure of the porous substrate to the oxyacetylene flame. Consequently, HEC-SiC5 exhibits the lowest mass and linear ablation rates among all samples, demonstrating that increasing the thickness of the SiC-rich dense layer through pore-structure regulation is an effective strategy for enhancing the ablation resistance of HEC-SiC ceramics.

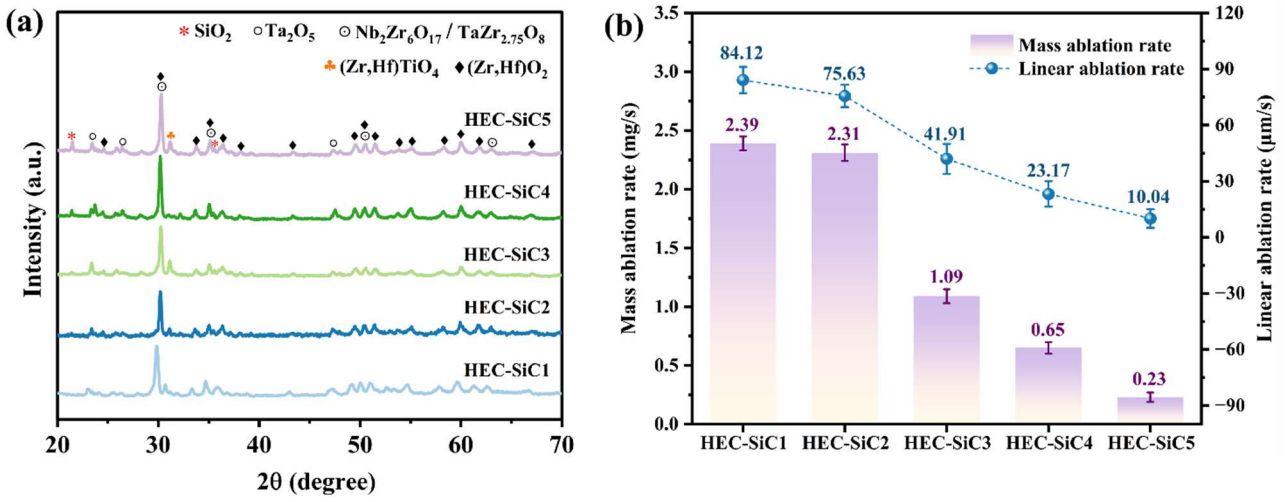


Figure 5. (**a**) XRD patterns of HEC-SiC1–HEC-SiC5 after ablation; (**b**) Mass and linear ablation rate.

Figure 6 shows the surface morphology of the ablation central regions of the HEC-SiC1–HEC-SiC5 samples after ablation. The ablation center generally exhibits a rough, porous morphology, but a gradual transition from a loose surface to a relatively smooth, continuous, oxide-covered surface can be observed as the thickness of the SiC-rich dense layer increases, particularly in HEC-SiC5.

For samples with a relatively thin SiC-rich layer, the amount of SiO_2 generated by SiC oxidation is insufficient to form a continuous, stable protective layer. As a result, the underlying HEC matrix is more

susceptible to oxidation under the high-temperature oxidizing environment, producing discontinuous and loosely packed transition-metal oxide products. The presence of pores and structural defects in this oxide layer facilitates oxygen transport to the underlying matrix, thereby promoting further oxidation.

In contrast, a thicker SiC-rich dense layer provides a greater SiC reservoir for oxidation and consequently promotes the generation of a larger amount of SiO_2 during ablation. Part of the molten SiO_2 can be retained on the ablation surface and interact with the transition-metal oxides generated from the HEC matrix, facilitating the formation of a relatively continuous protective oxide layer. The viscous flow of the oxide phase can seal surface pores and cracks, thereby reducing oxygen ingress and suppressing oxidation of the underlying HEC matrix. This surface-protection mechanism becomes increasingly pronounced with increasing thickness of the SiC-rich dense layer, resulting in improved ablation resistance.

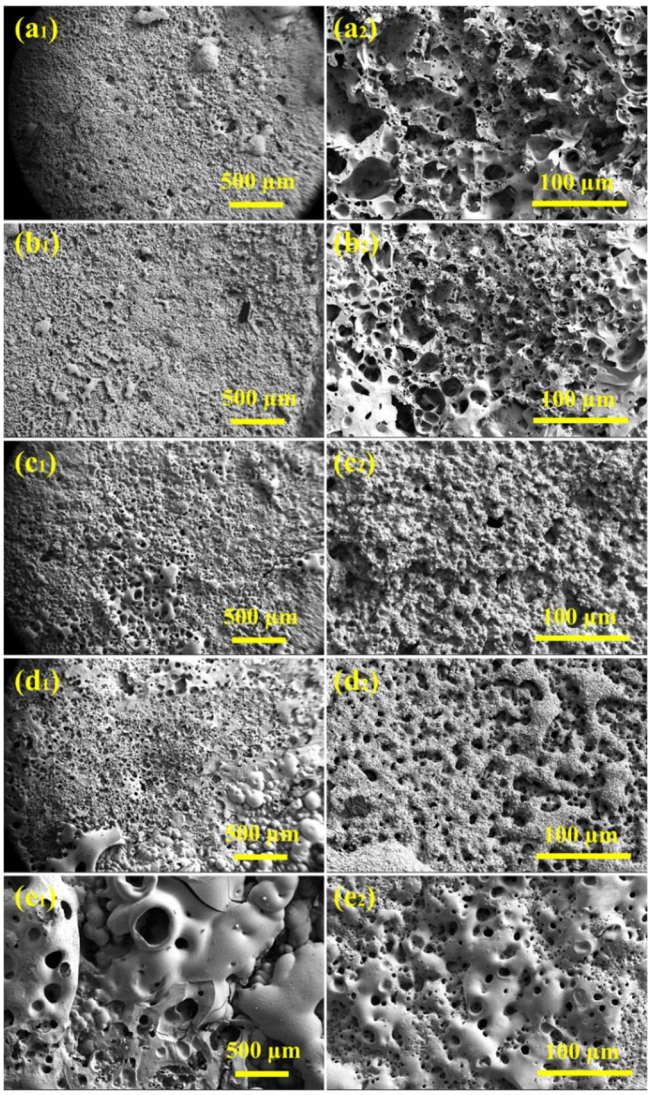


Figure 6. Surface microstructure of the central ablation region: (**a1**–**e1**) HEC-SiC1 to HEC-SiC5; (**a2**–**e2**) corresponding high-magnification images showing the evolution of the oxide layer and surface pore structure.

Figure 7 presents the cross-sectional elemental distribution maps of the ablation central regions of different HEC-SiC samples after ablation. It can be observed that the thickness of the oxide layer gradually decreases as the thickness of the SiC-rich dense layer increases. The quantitative measurements of the oxide-layer thickness are presented in Figure 8, which further confirms this decreasing trend. These results indicate that the SiC-rich dense layer effectively mitigates the oxidation damage of the underlying HEC matrix under extreme ablation conditions.

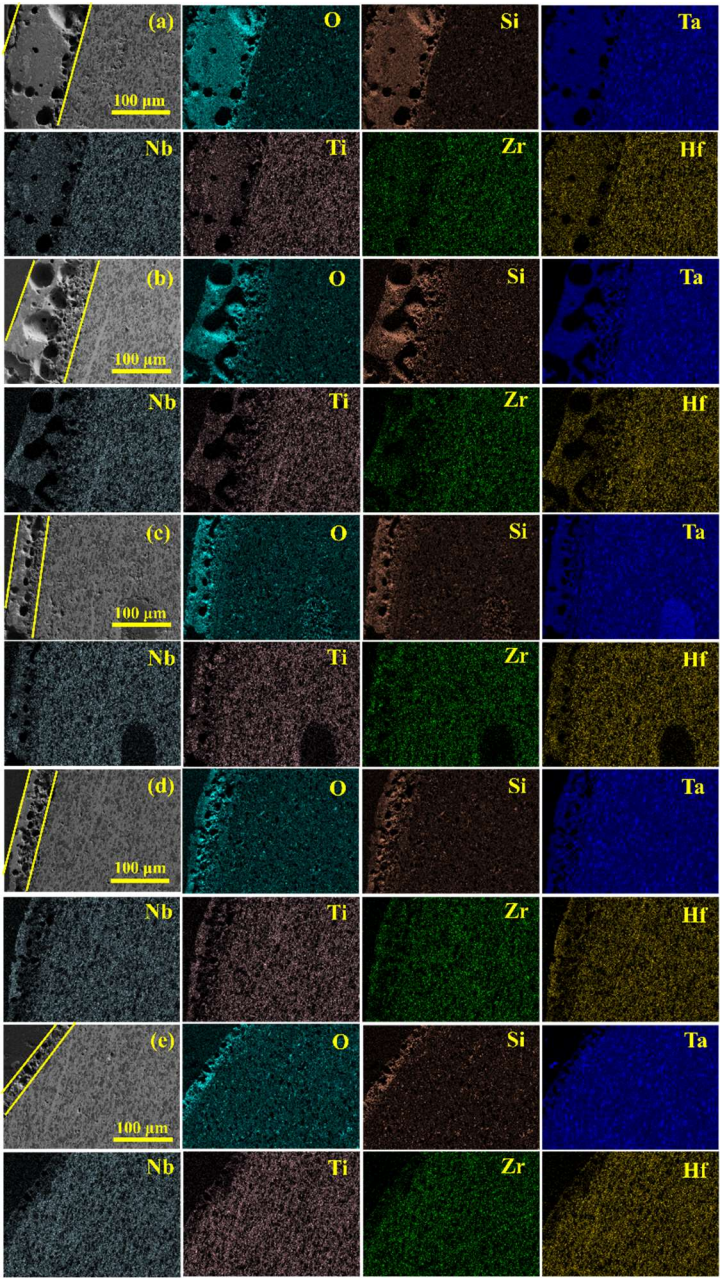


Figure 7. Cross-sectional SEM images and corresponding EDS elemental mappings of the central ablation region: (**a**) HEC-SiC1, (**b**) HEC-SiC2, (**c**) HEC-SiC3, (**d**) HEC-SiC4, and (**e**) HEC-SiC5, showing the oxide layer structure and elemental distribution.

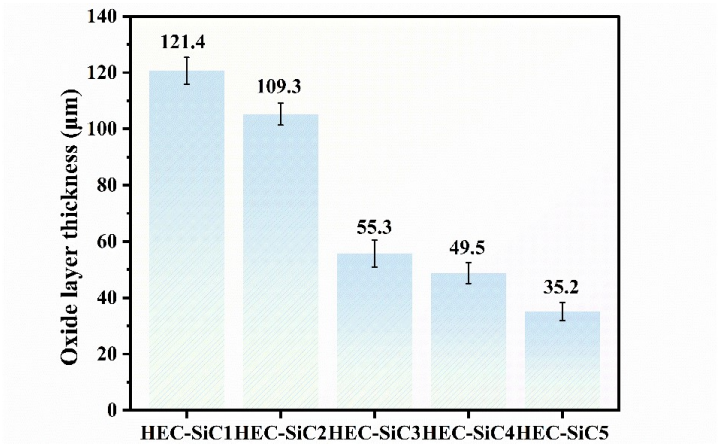


Figure 8. Average oxide layer thickness in the central ablation region of HEC-SiC1 to HEC-SiC5 after ablation.

This behavior is mainly attributed to the synergistic effect between the molten SiO_2 generated from SiC oxidation and the high-melting-point transition metal oxides derived from the HEC matrix (Ta, Nb, Ti, Zr, and Hf). These oxidation products interact to form a viscous and oxygen-diffusion-resistant composite oxide layer. The oxide layer maintains structural continuity at elevated temperatures and exhibits dynamic self-healing capability through viscous flow, thereby sealing surface cracks and pores. Consequently, the inward diffusion of oxygen is effectively inhibited, reducing the oxidation of the underlying HEC matrix. Therefore, with increasing SiC-rich dense layer thickness, the enhanced barrier effect of the SiC-derived oxide layer results in a reduced oxide-layer thickness after ablation.

Moreover, during the ablation process, oxidation of the HEC matrix continuously generates CO and CO_2 gases. In regions covered by relatively thin or discontinuous oxide films, these gaseous products can readily escape through structural defects, resulting in relatively efficient gas transport.

With increasing SiC content toward the surface, the build-up of a denser composite oxide layer may enhance the barrier effect and hinder the outward transport of gaseous products. As a result, CO/CO_2 generated during the oxidation of the carbide matrix may be partially trapped near the interface between the oxide layer and the unoxidized HEC matrix, which may contribute to the presence of concentrated closed pores. The presence of these closed pores suggests that the protective oxide layer influences gas transport and pore evolution during ablation, further indicating the role of the SiC-derived oxidation layer in regulating the ablation behavior of the HEC-SiC composites.

Figure 8 quantitatively compares the thicknesses of the oxide layers formed in the central ablation regions of the HEC-SiC1–HEC-SiC5 samples. As shown in Figure 8, the oxide-layer thickness decreases progressively with increasing thickness of the SiC-rich dense layer, decreasing from 121.4 μm for HEC-SiC1 to 104.9, 55.3, 49.5, and 35.2 μm for HEC-SiC2, HEC-SiC3, HEC-SiC4, and HEC-SiC5, respectively. Overall, the oxide-layer thickness is reduced by approximately 71.0% from HEC-SiC1 to HEC-SiC5. This pronounced decrease is consistent with the elemental distribution results shown in Figure 7 and quantitatively confirms that increasing the thickness of the SiC-rich dense layer effectively suppresses oxidation of the underlying HEC matrix during ablation.

Figure 9 illustrates the proposed ablation mechanism of the gradient-structured HEC-SiC composites. In the ablation center, the extremely high flame temperature decreases the viscosity of the SiO_2-rich oxide melt, making it more susceptible to volatilization and mechanical removal. Simultaneously, the high-velocity airflow hinders the development of a continuous and stable oxide layer, resulting in the most severe material loss in this region. In contrast, in the surrounding heat-affected zone where the temperature is relatively lower, the viscosity of the oxide melt increases and the erosive effect of the airflow weakens, facilitating the development and retention of a continuous oxide scale.

During ablation, oxidation of SiC generates SiO_2, while the oxidation of the high-entropy carbide matrix produces refractory transition-metal oxides. These oxide particles become incorporated into the SiO_2-rich melt and contribute to a particle-pinning effect, which enhances the stability and adherence of the oxide scale. In addition, the oxide melt can effectively fill pores and microcracks formed by gas evolution, thereby reducing oxygen transport to the underlying substrate.

With increasing thickness of the SiC-rich dense layer, more SiO_2 is produced during ablation, promoting the build-up of a thicker and more continuous SiO_2-rich composite oxide layer. This protective oxide scale provides a more effective barrier against oxygen diffusion and substrate oxidation, leading to a progressive decrease in oxide-layer thickness and a significant improvement in ablation resistance. Therefore, the enhanced ablation performance of the HEC-SiC composites can be primarily attributed to the synergistic effects of the SiC-rich dense layer and the protective composite oxide scale formed during ablation.

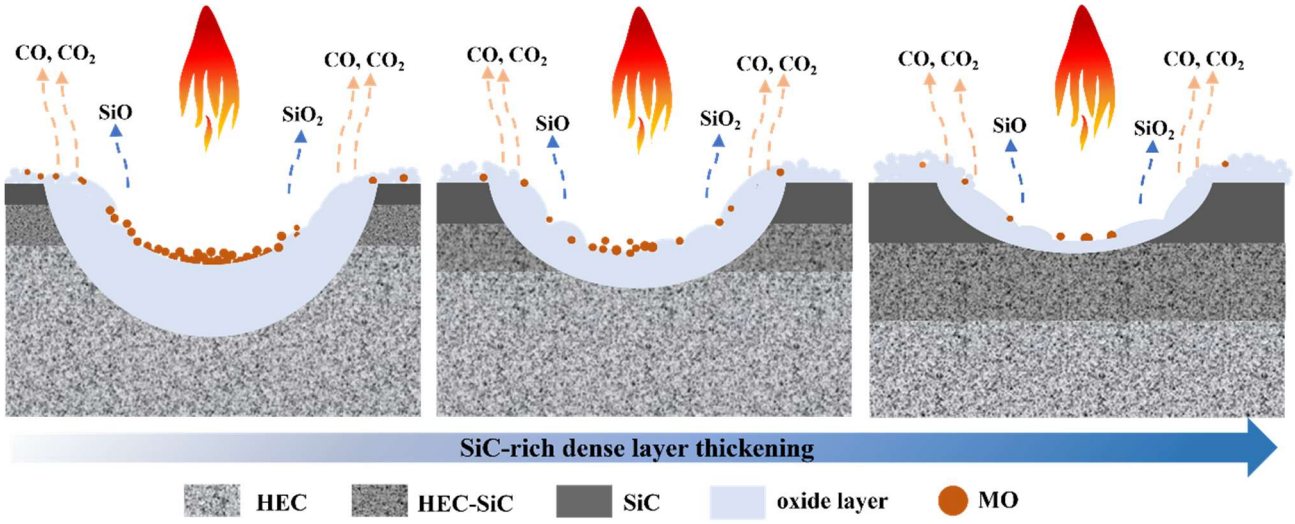


Figure 9. Schematic illustration of the influence of SiC-rich dense layer thickness on the ablation behavior of HEC-SiC composites.

4. Conclusions

In this work, a gradient-structured $(Ta_{0.2}Nb_{0.2}Ti_{0.2}Zr_{0.2}Hf_{0.2})C$-SiC composite was successfully fabricated by combining vacuum impregnation of phenolic resin followed by carbonization with reactive melt infiltration of Si. The resulting composite consists of a dense SiC-rich surface layer and a porous inner layer. The main conclusions are as follows:

(1) The initial porosity of the PHEC matrix strongly regulates molten Si infiltration and the growth of the SiC-rich dense layer. As the matrix porosity increased from 23.08% to 59.34%, the average thickness of the SiC-rich dense layer increased from 33.3 to 121.2 μm, indicating that the enlarged interconnected pore channels promoted molten Si infiltration and SiC formation.

(2) During ablation, oxidation of the SiC-rich layer generates molten SiO_2, which reacts with refractory oxides such as ZrO_2 and HfO_2 produced by oxidation of the HEC matrix, resulting in a composite oxide layer. With increasing SiC-rich layer thickness, the oxide layer becomes more continuous and compact, which further suppresses oxygen ingress and may hinder the outward transport of gaseous products, contributing to the development of concentrated closed pores near the oxide/unoxidized HEC interface.

(3) The growth of the SiC-rich dense layer and the evolution of the protective oxide layer are closely associated with the ablation performance. Among the investigated samples, HEC-SiC5, with the thickest SiC-rich dense layer of 121.2 μm, developed the most continuous and compact composite oxide layer (35.2 μm) and exhibited the best ablation resistance, with a mass ablation rate of 0.23 mg/s and a linear ablation rate of 10.04 μm/s. These results demonstrate that tailoring the initial pore structure of the porous HEC matrix provides an effective strategy for regulating Si infiltration, SiC-rich layer growth, and ultimately the ablation performance of porous HEC-based composites.

Author Contributions

Writing—Original Draft Preparation, X.W.;Writing—Review&Editing, C.L., H.O.; Conceptualization, X.W., C.L., H.O., Q.Y., T.S.; Validation, C.L., H.O., Q.Y., T.S.; Investigation, X.W., Q.Y.; Supervision, C.L., H.O., T.S.; Funding Acquisition, C.L., H.O.; Methodology, X.W.,Q.Y., T.S.

Ethics Statement

Not applicable.

Informed Consent Statement

Not applicable.

Data Availability Statement

Data will be made available on request.

Funding

This work was supported by the National Natural Science Foundation of China (Grant No. 52173299, 52372087), Natural Science Foundation of Shaanxi Province (Grant No. 2025SYS-SYSZD-062).

Declaration of Competing Interest

The authors declare that they have no known competing financial interests or personal relationships that could have appeared to influence the work reported in this paper.

References

1. Ding Y, Yue X, Chen G, Si J. Review of control and guidance technology on hypersonic vehicle. *Chin. J. Aeronaut.* **2022**, *35*, 1–18. DOI:10.1016/j.cja.2021.10.037
2. Sziroczak D, Smith H. A review of design issues specific to hypersonic flight vehicles. *Prog. Aerosp. Sci.* **2016**, *84*, 1–28. DOI:10.1016/j.paerosci.2016.04.001
3. Uyanna O, Najafi H. Thermal protection systems for space vehicles: A review on technology development, current challenges and future prospects. *Acta Astronaut.* **2020**, *176*, 341–356. DOI:10.1016/j.actaastro.2020.06.047
4. Zhang Y, Liu B, Zhang X, Liu H, Wang X, Zhang Y, et al. Advanced characterization techniques and protective mechanism investigation methodologies for ultra-high temperature thermal protective materials. *Prog. Mater. Sci.* **2027**, *164*, 101788. DOI:10.1016/j.pmatsci.2026.101788
5. Guria J, Bansal A, Kumar V. Effect of additives on the thermal conductivity of zirconium diboride based composites-A review. *J. Eur. Ceram. Soc.* **2021**, *41*, 1–23. DOI:10.1016/j.jeurceramsoc.2020.08.051
6. Shen T, Li C, Ouyang H, Wang J, Bao L, Wu S, et al. Enhancing the ablation resistance of C/C-HfC-ZrC-SiC composites via a molten-salt-deposited TiC coating. *Ceram. Int*. **2026**, *52*, 14346–14357. DOI:10.1016/j.ceramint.2026.02.072
7. Serrano NL, Ruiz L, Doolittle CT, Burk D, Ghoshal A, Walck S, et al. Properties and high-temperature ablation behavior of pressureless sintered HfC-SiC-TaC ceramics. *J. Am. Ceram. Soc*. **2025**, *109*, 70357. DOI:10.1111/jace.70357
8. Mishra R, Singh V, Patel M, Mitra R. Thermal shock resistance and long-term ablation behaviour of the Cf-ZrB_2-SiC UHTCMCs fabricated via slurry infiltration and hot pressing. *J. Eur. Ceram. Soc.* **2026**, *46*, 118650. DOI:10.1016/j.jeurceramsoc.2026.118650
9. Zeng Y, Wang D, Xiong X, Zhang X, Withers P, Sun W, et al. Ablation-resistant carbide $Zr_{0.8}Ti_{0.2}C_{0.74}B_{0.26}$ for oxidizing environments up to 3000 °C. *Nat. Commun.* **2017**, *8*, 15836. DOI:10.1038/ncomms15836
10. Ni D, Cheng Y, Zhang J, Liu J, Zou J, Chen B, et al. Advances in ultra-high temperature ceramics, composites, and coatings. *J. Adv. Ceram.* **2022**, *11*, 1–56. DOI:10.1007/s40145-021-0550-6
11. Li K, Guo L, Wang J, Chen H, Li Y, Zhang R. Synergistic enhancement of strength and ablation resistance in HEC ceramics by SiC and short carbon fiber reinforcement. *Surf. Interf.* **2026**, *86*, 108714. DOI:10.1016/j.surfin.2026.108714
12. Sengupta P, Manna I. Advanced High-Temperature Structural Materials for Aerospace and Power Sectors: A Critical Review. *Trans. Indian Inst. Met.* **2019**, *72*, 2043–2059. DOI:10.1007/s12666-019-01598-z
13. Zhang X, Guo L, Liu H, Zhang Y, Fu Q, Yin X, et al. Advanced anti-ablation C/C composites: structural design strategies and future perspective. *Mater. Today*. **2024**, *80*, 710–736. DOI:10.1016/j.mattod.2024.09.004
14. Wang Y, Csanadi T, Zhang H, Dusza J, Reece M, Zhang R. Enhanced hardness in high-entropy carbides through atomic randomness. *Adv*. *Theory*. *Simul.* **2020**, *3*, 2000111. DOI:10.1002/adts.202000111
15. Castle E, Csanádi T, Grasso S, Dusza J, Reece M. Processing and properties of high-entropy ultra-high temperature carbides. *Sci*. *Rep.* **2018**, *8*, 8609. DOI:10.1038/s41598-018-26827-1
16. He H, Yang J, Guo W, Zhang S, Bai S. Microstructures and formation mechanism of continuous carbon fiber-reinforced (TiZrHfNbTa)C high-entropy ceramic composites fabricated via high-entropy alloy reactive melt infiltration. *Ceram. Int.* **2023**, *49*, 36997–37008. DOI:10.1016/j.ceramint.2023.09.032

17. Harrington T, Gild J, Sarker P, Toher C, Rost C, Dippo O, et al. Phase stability and mechanical properties of novel high entropy transition metal carbides. *Acta Mater.* **2019**, *166*, 271–280. DOI:10.1016/j.actamat.2018.12.054
18. Shen T, Li C, Ouyang H, He M, Wu S, Liu J, et al. Tailoring of PyC/TiC interface for Cf/(TiZrHfNbTa)C-SiC composites with enhanced mechanical performance and durability in extreme environments. *J. Mater. Sci. Technol*. **2026**, *270*, 267–278. DOI:10.1016/j.jmst.2026.01.046
19. Demirskyi D, Borodianska H, Suzuki T, Sakka Y, Yoshimi K, Vasylkiv O. High-temperature flexural strength performance of ternary high-entropy carbide consolidated via spark plasma sintering of TaC, ZrC and NbC. *Scr. Mater.* **2019**, *164*, 12–16. DOI:10.1016/j.scriptamat.2019.01.024
20. Zhou J, Zhang J, Zhang F, Niu B, Lei L, Wang W. High-entropy carbide: a novel class of multicomponent ceramics. *Ceram. Int.* **2018**, *44*, 22014–22018. DOI:10.1016/j.ceramint.2018.08.100
21. Wang Y, Reece M. Oxidation resistance of (Hf-Ta-Zr-Nb)C high entropy carbide powders compared with the compo-nent monocarbides and binary carbide powders. *Scr. Mater.* **2021**, *193*, 86–90. DOI:10.1016/j.scriptamat.2020.10.038
22. Ni N, Ding Q, Shi Y, Jiang J , Li L, Zhang R, et al. Ablation behavior of high-entropy carbides ceramics ($Hf_{0.2}Zr_{0.2}Ta_{0.2}Nb_{0.2}Ti_{0.2}$)C upon exposition to an oxyacetylene torch at 2000 °C. *J. Eur. Ceram. Soc.* **2023**, *43*, 2306–2319. DOI:10.1016/j.jeurceramsoc.2023.01.017
23. Ye B, Wen T, Chu Y. High-temperature oxidation behavior of ($Hf_{0.2}Zr_{0.2}Ta_{0.2}Nb_{0.2}Ti_{0.2}$)C high-entropy ceramics in air. *J. Am. Ceram. Soc*. **2020**, *103*, 500–507. DOI:10.1111/jace.16725
24. Peng Z, Sun W, Xiong X, Zhang H, Guo F, Li J. Novel refractory high-entropy ceramics: Transition metal carbonitrides with superior ablation resistance. *Corros. Sci.* **2021**, *184*, 109359. DOI:10.1016/j.corsci.2021.109359
25. Jin X, Fan X, Lu C, Wang T. Advances in oxidation and ablation resistance of high and ultra-high temperature ceramics modified or coated carbon/carbon composites. *J. Eur. Ceram. Soc.* **2018**, *38*, 1–28. DOI:10.1016/j.jeurceramsoc.2017.08.013
26. Zhang B, Yin J, Zheng J, Liu X, Huang Z, Dusza J, et al. High temperature ablation behavior of pressureless sintered $Ta_{0.8}Hf_{0.2}C$-based ultra-high temperature ceramics. *J. Eur. Ceram. Soc.* **2020**, *40*, 1784–1789. DOI:10.1016/j.jeurceramsoc.2019.11.043
27. Liu T, Niu Y, Li C, Pan X, Shi M, Zheng X, et al. Ablation resis-tance of ZrC-$MoSi_2$/ZrC-SiC double-layered coating in a plasma flame. *Corros. Sci.* **2018**, *145*, 239–248. DOI:10.1016/j.corsci.2018.10.006
28. Zhang X, Sun Y, Guo L, Liu H, Liu T, Fu Q, et al. Bioinspired vacuum-driven approach enables mechanically robust, ablation-resistant sharp leading-edge composites. *Mater. Today* **2026**, *92*, 126–139. DOI:10.1016/j.mattod.2025.11.031
29. Shen T, Li C, Ouyang H, He M, Wu S, Bao L, et al. A mortise-tenon joint inspired interface structure design for synergistically enhancing the mechanical properties and thermal shock resistance of Cf/(HfNbTaTiZr)C-SiC composites. *J. Adv. Ceram*. **2026**, *15*, 9221227. DOI:10.26599/jac.2025.9221227
30. Li W, Cui C, Bao J, Zhang G, Li S, Wang G. Properties regulation of SiC ceramics prepared via stereolithography combined with reactive melt infiltration techniques. *Ceram. Int*. **2021**, *47*, 33997–34004. DOI:10.1016/j.ceramint.2021.08.307
31. Makurunje P, Sigalas I, Binner J. Scale characterisation of an oxidised (Hf, Ti)C-SiC ultra-high temperature ceramic matrix composite. *J. Eur. Ceram. Soc.* **2021**, *41*, 167–175. DOI:10.1016/j.jeurceramsoc.2020.08.048
32. Cai F, Ni D, Chen B, Ye L, Sun Y, Lu J, et al. Fabrication and properties of Cf/($Ti_{0.2}Zr_{0.2}Hf_{0.2}Nb_{0.2}Ta_{0.2}$)C-SiC high-entropy ceramic matrix composites via precursor infiltration and pyrolysis. *J. Eur. Ceram. Soc.* **2021**, *41*, 5863–5871. DOI:10.1016/j.jeurceramsoc.2021.05.026
33. Liu R, Yang L, Miao H, Jiang M, Wang Y, Liu X, et al. Influence of the SiC matrix introduction time on the microstructure and mechanical properties of Cf/$Hf_{0.5}Zr_{0.5}$C-SiC ultra-high temperature composites. *Ceram. Int*. **2022**, *48*, 3762–3770. DOI:10.1016/j.ceramint.2021.10.159
34. Zhang Y, Wang X, Liu B, Zhang M, Fu Q, Yin X, et al. Bioinspired C/C composites with long-duration ablation resistance for thermal protection up to 2400 °C. *Mater. Sci. Eng. R Rep*. **2026**, *168*, 101157. DOI:10.1016/j.mser.2025.101157
35. Williams P, Sakidja R, Perepezko J, Ritt P. Oxidation of ZrB_2-SiC ultra-hightemperature composites over a wide range of SiC content. *J. Eur. Ceram. Soc.* **2012**, *32*, 3875–3883. DOI:10.1016/j.jeurceramsoc.2012.05.021
36. Shen T, Li C, Ouyang H, He M, Wu S, Wang L, et al. High-entropy ($Ta_{0.2}Nb_{0.2}Ti_{0.2}Hf_{0.2}Zr_{0.2}$)C-SiC Ceramics: Achieving Superior Ablation Resistance through SiC Particle Size Optimization. *J. Eur. Ceram. Soc.* **2026**, *46*, 117800. DOI:10.1016/j.jeurceramsoc.2025.117800
37. Wang H, Cao Y, Liu W, Wang Y. Oxidation behavior of (HfTaZrTiNb)C-xSiC ceramics at high temperature. *Ceram. Int.* **2020**, *46*, 11160–11168. DOI:10.1016/j.ceramint.2020.01.137
38. Lu K, Liu J, Wei X, Bao W, Wu Y, Li F, et al. Microstructures and mechanical properties of high-entropy ($Ti_{0.2}Zr_{0.2}Hf_{0.2}Nb_{0.2}Ta_{0.2}$)C ceramics with the addition of SiC secondary phase. *J. Eur. Ceram. Soc.* **2020**, *40*, 1839–1847. DOI:10.1016/j.jeurceramsoc.2019.12.056

39. Yang L, Dong S, Cui T, Xin J, Chen G, Hong C, et al. Novel gradient ZrB_2-$MoSi_2$-SiC dense layer with enhanced emissivity and long-term oxidation resistance at ultra-high temperatures. *Rare Met.* **2025**, *44*, 2043–2058. DOI:10.1007/s12598-024-02959-4
40. Zhao T, Dai J, Su C, Shi Y, Sha J. Microstructure and Ablation Resistance of C/C Composites Modified by Hf-Si-based Coating-matrix Integrated Structure Fabricated by Reactive Melt Infiltration. *J. Inorg. Mater*. **2026**, *41*, 583–594. DOI:10.15541/jim20250424
41. Yang Q, Li C, Ouyang H, Gao R, Shen T, Huang J. Dual-porosity $(Ta_{0.2}Nb_{0.2}Ti_{0.2}Zr_{0.2}Hf_{0.2})C$ high-entropy ceramics with high compressive strength and low thermal conductivity prepared by pressureless sintering. *Materials* **2023**, *16*, 2495. DOI:10.3390/ma16062495